NO Detection on Exposed Fe–N4 Sites Deposited on Nanometer-Sized Cu-Hemin MOFs Coated on Reduced Graphene Oxide at Room Temperature

Wu, You; Li, Weiran; Chang, Yanwei; Gao, Yixun; Wang, Fengnan; Li, Hao; French, Paddy J.; Lee, Yi Kuen; Wang, Yao; More Authors

DOI
10.1021/acsanm.4c06397

Publication date
2025

Document Version
Final published version

Published in
ACS Applied Nano Materials

Citation (APA)
Wu, Y., Li, W., Chang, Y., Gao, Y., Wang, F., Li, H., French, P. J., Lee, Y. K., Wang, Y., & More Authors (2025). NO Detection on Exposed Fe–N4 Sites Deposited on Nanometer-Sized Cu-Hemin MOFs Coated on Reduced Graphene Oxide at Room Temperature. *ACS Applied Nano Materials*, *8*(14), 6943-6954. https://doi.org/10.1021/acsanm.4c06397

ACS APPLIED NANO MATERIALS

www.acsanm.org Article

NO Detection on Exposed Fe−N_4 Sites Deposited on Nanometer-Sized Cu-Hemin MOFs Coated on Reduced Graphene Oxide at Room Temperature

You Wu, Weiran Li, Yanwei Chang, Yixun Gao, Fengnan Wang, Hao Li, Paddy J. French, Yi-Kuen Lee, Sheikh A. Akbar, Ahmad M. Umar Siddiqui, Yao Wang,* and Guofu Zhou

Cite This: ACS Appl. Nano Mater. 2025, 8, 6943−6954 Read Online

ACCESS | Metrics & More | Article Recommendations | Supporting Information

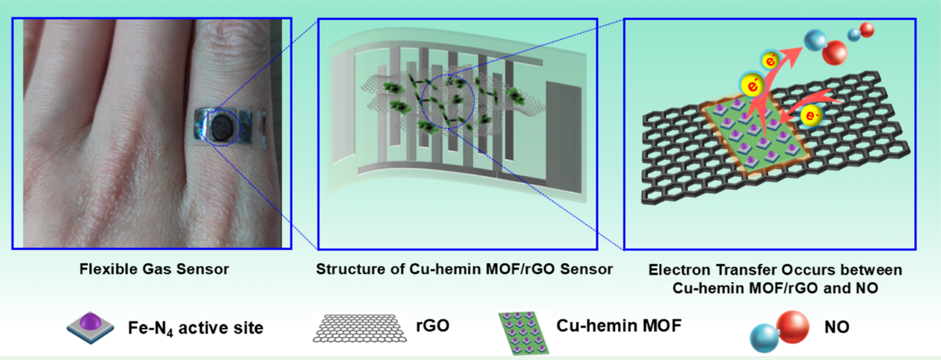

ABSTRACT: For the practical diagnosis of inflammatory respiratory diseases, achieving sensitive and rapid NO sensing at the parts per billion level, all at room temperature, is of great significance. Herein, we developed a chemiresistor gas sensor with a sheet-on-sheet structure composed of an amorphous Cu-hemin MOF with reduced graphene oxide (rGO) nanosheets. The SEM images show that the Cu-hemin MOF/rGO composite exhibits a two-dimensional sheet-like structure. Due to its nanosized architecture, the Cu-hemin MOF exhibits a significant number of active sites for efficient NO detection. The Cu-hemin MOF/rGO composite material exhibited excellent NO sensing performance, including high sensitivity (R_a/R_g = 1.06, 50 ppb), reliable repeatability, high selectivity, and fast response/recovery (43 s/367 s, 10 ppm). The mechanism study revealed that the formation of the MOF altered the hemin dimer's structure, resulting in the release of additional Fe(III)−N_4 active sites and improved sensitivity. Moreover, the incorporation of rGO significantly boosted the conductivity of Cu-hemin MOFs. Using this two-dimensional sheet-like material, a mask-type sensor was also prepared and verified to be effective as a flexible and wearable sensing device for parts per billion level exhaled NO detection.

KEYWORDS: *nitric oxide, hemin MOF, graphene, room temperature, chemiresistive gas sensor*

1. INTRODUCTION

Analyzing specific gases exhaled by the human body as a noninvasive method for disease diagnosis is one of the research directions in modern medicine.[1,2] Nitric oxide (NO), an active small molecule, is of great significance in human physiological activities and is considered to be closely associated with human health.[3] In clinical analysis, fractional exhaled nitric oxide (FeNO, ppb-level) is one of the typical biological markers used to detect airway inflammation diseases such as asthma and chronic cough.[4−6] The content of NO is generally found to be more than 50 ppb in exhaled gases from suspected patients suffering from airway inflammation.[7−9] Therefore, the detection of parts per billion-level NO is of great significance for clinical diagnosis of respiratory diseases. However, due to the high reactivity and oxidizing ability of NO (which is lower than NO_2 but higher than other nonoxidizing gases), meeting the increasing clinical demand for NO gas sensors remains a significant challenge.[10]

Up to now, various gas sensors have been developed to achieve highly sensitive and selective performance toward NO molecules, such as mass spectrometry,[11] gas chromatography,[12] and surface-enhanced Raman scattering technique.[13] Regrettably, these systems are dependent on large, expensive instruments, which pose significant challenges in meeting the

Received: December 16, 2024
Revised: March 26, 2025
Accepted: March 27, 2025
Published: April 2, 2025

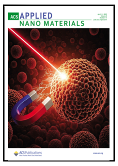

https://doi.org/10.1021/acsanm.4c06397
ACS Appl. Nano Mater. 2025, 8, 6943−6954

requirements for simple, compact, and cost-effective disease diagnostics. Recently, chemiresistive gas sensors, mainly utilizing metal oxide semiconductors (MOSs), such as ZnO,[14,15] WO_x,[16] SnO_x,[17] etc., is a hot topic in gas sensing researches. These gas sensors show good performance with fast response time and easy preparation; also, they are applicable in integrated circuit systems. Nevertheless, at room temperature (RT), the vast majority of MOS-based NO sensors exhibit low electrical conductivity and poor surface activity. Consequently, they necessitate a relatively high operating temperature (generally >180 °C) to activate the oxygen species. These species can only be produced via a heating process.[18−20] These shortcomings limit their potential for application in RT environments. Therefore, the development of a RT chemiresistive NO sensor that meets the requirements of respiration monitoring is essential.

In recent years, it has been found that NO can be specifically recognized by the metal−N_4 active site in a RT environment.[21] Iron porphyrin and hemin with Fe−N_4 groups are naturally more ideal materials for RT detection of NO.[22−27] However, iron porphyrin hemin molecules interact via $\pi-\pi$ stacking and exhibit a strong tendency to self-aggregate, which predisposes them to dimer formation. Self-aggregation of hemin results in the iron atoms of the Fe−N_4 unit being occupied by Fe−O coordination bonds, which prevents them from interacting with NO molecules.[28,29] Thus, only a few Fe(III)−N_4 units are unoccupied and free to interact with NO molecules. It is necessary to prevent the formation of hemin-dimers and disrupt the crystal structure.

Metal−organic skeletons (MOFs), as a new type of organic semiconductor material, can effectively prevent the self-aggregation of ligands because of their fine crystallinity and predictable periodic scaffold structure of metal and ligand. Therefore, it can be beneficial to prevent hemin from forming self-polymerization by constructing a regular structure. MOFs also combine the advantages of organic and inorganic components, featuring high porosity and a large specific surface area, making them attractive as sensing materials.[30] In 2023, Chang et al. designed and synthesized a porphyrin-based MOF with a rod-like morphology, which was then assembled with MXene ($Ti_3C_2T_x$) via hydrogen bonding to provide a chemically resistant NO sensing hybrid (Co-TCPP(Fe)/$Ti_3C_2T_x$) with excellent NO sensing performance including a practical limit of detection (pLOD) of 100 ppb.[31] In 2024, Chang et al. prepared a heterojunction with a sheet-on-sheet (SOS) structure using a sheeted porphyrin MOF DLS-2D-Co-TCPP(Fe) with 5-aminonaphthalene-1-sulfonic acid-rGO (ANS-rGO) nanosheets, which was used to carry out room-temperature NO detection with a detection line capable of reaching 250 ppb. However, the pLOD is still not enough for practical disease detection.[32]

Based on this sheet-on-sheet MOF-constructing strategy, we found Cu-TCPP-based MOFs have great potential for the development of high-performance gas sensors since they have a larger specific surface area, more adequate active sites, and fast electron transfer reaction.[33,34] Moreover, Cu^{2+}, serving as the bridging metals in the MOF, plays an important role in preventing the formation of dimers of hemin molecules, which would otherwise hinder the exposure of Fe−N_4 active sites. This is a required process for the improvement of the gas sensing performance.[35] Ma et al. assembled a two-dimensional Cu-TCPP metal−organic skeleton (MOS) nanomembrane and G-tetrastranded heme chloride DNAenzyme to construct a electrochemical hydrogen peroxide (H_2O_2) sensor directly.[36] Xiao et al. used 2D Cu-TCPP(Fe) as a nanoenzyme to modify the electrode surface for realizing the sensitive detection of sulfonamides.[37] These works have given us great inspiration. As far as we are aware, there is no published report on the correlation between the NO sensing performance and ordered dispersion of Fe−N_4 active sites in hemin-MOF.

In this work, in order to disrupt the hemin dimer structure and release more Fe(III)−N_4 active sites to improve the NO sensing performance of hemin-based chemiresistive sensors, a composite of an amorphous Cu-hemin MOF with reduced graphene oxide (rGO) nanosheets was prepared. A sheet-on-sheet structure was formed between Cu-hemin MOF and rGO. The Cu-hemin MOF has a nanoscale structure, which enhances its surface area and increases the number of active sites for efficient NO sensing. It can effectively prevent the formation of dimers between hemin. Excitingly, the sensor exhibited excellent NO detection at RT, especially with practical detection limits as low as 50 ppb. The mechanism analysis suggested that the enhanced NO sensing properties were attributed to the formation of the Cu-hemin MOF, which inhibited the dimerization of hemin molecules and disrupted the crystallization of hemin. Furthermore, a wearable sensing device incorporating Cu-hemin MOF/rGO was developed, and its testing demonstrated notable performance, highlighting its potential for advancing the next generation of wearable and intelligent electronic devices.

2. EXPERIMENTAL SECTION

2.1. Materials. The flake-like graphite (325 mesh, ≥99.6%) and other chemicals were purchased from XianFeng NANO Co., Ltd. (Nanjing, P. R. China) and Shanghai Titanchem Co., Ltd. (Shanghai, P. R. China), respectively. Ag−Pd interdigitated electrodes (IDEs) and platinum target (0.3 mm thickness) were obtained from Beijing Elite Tech Co., Ltd. (Beijing, P. R. China) and Hefei Kejing Material Technology Co., Ltd. (China), respectively.

2.2. Graphene Oxide Preparation. GO was obtained following the previous method.[10] To begin, 1 g of natural graphite was added to 23 mL of concentrated sulfuric acid, and the mixture was stirred for 50 min while maintaining the reaction temperature between −1 and 1 °C. Gradually, 6 g of $KMnO_4$ was added in portions, and stirring continued at low temperature for 3 h. The reaction mixture was then transferred to a 40 °C constant-temperature bath and stirred for 45 min. Afterward, the reaction was moved to an 80 °C water bath, where 80 mL of distilled water was added in portions, followed by stirring for 15 min. An additional 60 mL of distilled water was then introduced. Subsequently, a mixture of 10.81 mL of 30% hydrogen peroxide and 60 mL of distilled water was slowly added. Finally, the product was washed and centrifuged, yielding a yellow graphene oxide solution. The measured concentration of GO was 5.8 mg/mL.

2.3. Preparation of Sensing Materials. The Cu-hemin MOF/rGO nanocomposites were obtained using a typical one-pot construction method. First, solution A was freshly prepared with 30 mg of hemin, which was dispersed in 5 mL of anhydrous ethanol with sonication for 10 min. Then $Cu(NO_3)_2{\cdot}2.5H_2O$ of different molar ratios was dissolved in 10 mL of anhydrous ethanol as solution B. Next, before GO was added, solution B was mixed with solution A under vigorous stirring for 2.0 h at RT. 1 mL of GO dispersion then was dropped into the mixture, and another sonication of 5 min was carried out. The solution obtained from the previous step was first refluxed in a mixture at 80 °C for 12 h. Subsequently, it was transferred into a 25 mL autoclave and subjected to a further solvothermal reaction at 120 °C for 4 h. Upon reaching ambient temperature after cooling, the synthesized product was subjected to vacuum filtration and rinsed 5 times alternately with DMF and DI water to remove the unreacted and remaining hemin or $Cu(NO_3)_2$.

Finally, the Cu-hemin MOF/rGO solution was redispersed in 10 mL of anhydrous ethanol through gentle sonication. To compare the gas sensing performance, rGO and hemin/rGO were prepared following the same procedure, except that $Cu(NO_3)_2$ was not added for the preparation of rGO, and hemin was omitted when preparing rGO without adding hemin for hemin/rGO synthesis. Besides, the control groups were obtained by employing DI water, DMF, and DMSO as solvents. With the exception of ethanol substitution, the control groups were fabricated through the same methodology employed for Cu-hemin MOF/rGO preparation.

2.4. Fabrication of the NO Sensor Based on Ag–Pd IDEs. The IDEs were sonicated with anhydrous ethanol and acetone for 30 min to remove surface contaminants before use. The NO sensing chip based on IDEs was prepared using the drop-drying method, following the procedure reported in the previous works.[10,27]

2.5. Fabrication of the Flexible NO Sensor. The PET and PDMS substrates were successively rinsed with deionized water, anhydrous ethanol, and acetone and subsequently dried using a stream of nitrogen gas. The 100 nm thick Pt layers were deposited on the flexible substrates with a similar electrode structure to IDEs through a metal pattern plate via the magnetron sputtering for 3 min (Figure S1).

2.6. Gas-Sensing Measurement. The gas-sensing measurement of the obtained materials followed the previous procedures at RT (25 ± 3 °C).[10] In this work, the response is defined as response = R_a/R_g, where R_a and R_g represent the sensing materials' resistance captured in N_2 and target gases, respectively. The response/recovery times are defined as the time required for IDEs exposure to/away from target gas until the resistance reaches/returns 90% of the response. The LOD is defined as the minimum concentration of the target gas that can be differentiated from the ambient atmosphere.

2.7. Characterizations. The preparation of samples for SEM, X-ray diffraction (XRD), FT-IR, Raman spectra, UV–vis, and X-ray photoelectron spectroscopy (XPS) followed the previous procedures.[27] Relative humidity (RH) was also regulated in the same manner as the reported one.[10]

3. RESULTS AND DISCUSSION

3.1. Surface and Structure Characterizations. The schematic illustration of the preparation of Cu-hemin MOF/rGO nanocomposites is displayed in Figure 1. First, $Cu(NO_3)_2 \cdot 2.5H_2O$ and hemin were dispersed in ethanol, and then graphene oxide was added with vigorous stirring and then refluxed at 80 °C for 12 h. Subsequently, the mixtures were transferred to autoclave for hydrothermal reaction, and finally Cu-hemin MOF/rGO nanocomplexes were obtained. The SEM images of hemin/rGO and Cu-hemin MOF/rGO nanocomposites are shown in Figure 2. It can be seen from Figure 2a,b that large hemin aggregates with a crystal-like morphology in the hemin/rGO were observed, which means plenty of $Fe-N_4$ active sites were occupied by carboxyl groups of adjacent hemin molecules.[10] Figure 2c,d presents the morphology of Cu-hemin MOF/rGO. It can be clearly seen that the Cu-hemin MOF had a loose, flaky structure, which combined well with rGO and was evenly dispersed on the rGO surface. A sheet-on-sheet nanoscale structure between Cu-hemin MOF and rGO can be clearly observed by the SEM image. The Cu-hemin MOF nanosheets have a size of approximately 500 nm, which contributes to their high surface area and enhanced reactivity. This is favorable for enhancing the surface area and edge sites for the NO adsorption. Meanwhile, the element distribution of the Cu-hemin MOF sheet was revealed by EDS element analysis (Figure 2e). Different elements, including C, N, O, Fe, and Cu, display uniform distributions on the surface of the Cu-hemin MOFs. Obviously, the Fe and Cu elements were uniformly distributed on the Cu-hemin MOF sheets region. These results clearly demonstrate the successful preparation of the Cu-hemin MOF composite with rGO and the uniform dispersion of the Cu-hemin MOF on rGO.

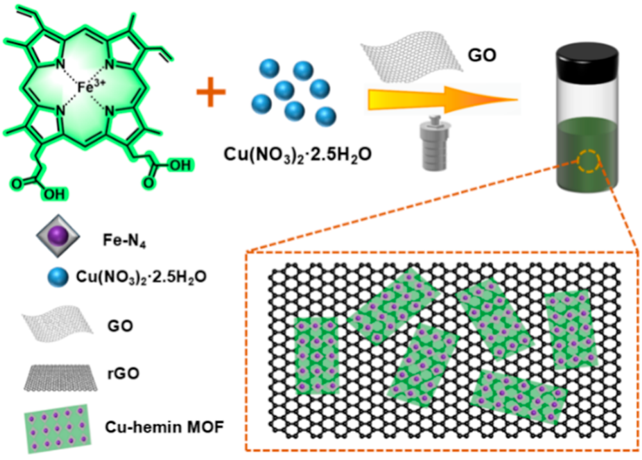

Figure 1. Schematic illustrations of the Cu-hemin MOF/rGO sensing material preparation.

A linkage was proposed between Cu^{2+} and carboxyl groups of hemins. The above Cu-hemin MOFs are thought to be formed via, which was helpful to disrupt the crystallization of hemin and release more $Fe-N_4$ active sites to interact with NO molecules. To confirm this, XRD, Fourier-transform infrared (FT-IR) spectroscopy, and UV–vis spectroscopy were utilized to characterize the MOF. Figure 3a shows the XRD curves of rGO, hemin/rGO, and Cu-hemin MOF/rGO. The XRD pattern of rGO showed a broad diffraction peak at approximately 23°, indicating the successful reduction of GO to rGO.[38] In XRD of Cu-hemin MOF/rGO, we believe that the peak appearing at 24° can be attributed to the (004) surface of Cu.[39] The sharp peaks of hemin/rGO distributed consistently with that of the previously reported hemin crystal aggregates, which proved the high crystallinity of hemin.[40] Compared with hemin/rGO, the peak distribution of Cu-hemin MOF/rGO is different and new peaks appeared in different locations. The first two peaks at 6.75 and 11.52° and the diffraction peaks at 20 and 30° are similar to the XRD patterns of metal-hemin MOF and other 2D MOF nanosheets reported by predecessors,[41−47] suggesting that the nanostructures were crystalline materials and the presence of Cu-hemin MOFs was confirmed.

As depicted in Figure 3b, the FT-IR spectra of rGO did not display the characteristic band corresponding to the C═O stretching vibration of the carboxyl group. This observation further confirms the successful reduction process. Moreover, Cu-hemin MOF/rGO and hemin/rGO both exhibited the typical peaks of both hemin and rGO in the FT-IR spectra. Compared to hemin/rGO, the peak at 1706 cm^{-1}, which corresponds to the stretching vibration of C═O, shows a decrease in intensity in the Cu-hemin/rGO composite. This can be interpreted as a result of coordination between Cu^{2+} and the carboxyl group.[33] The primary driving force behind the self-assembly is presumably the $\pi-\pi$ interaction between the conjugated structure of the porphyrin ring and the rGO nanosheets.[48] In hemin/rGO, the signal at 1577 cm^{-1} can be considered as the characteristic peak of C═C, while in the infrared spectrum of Cu-hemin/rGO, the C═C characteristic

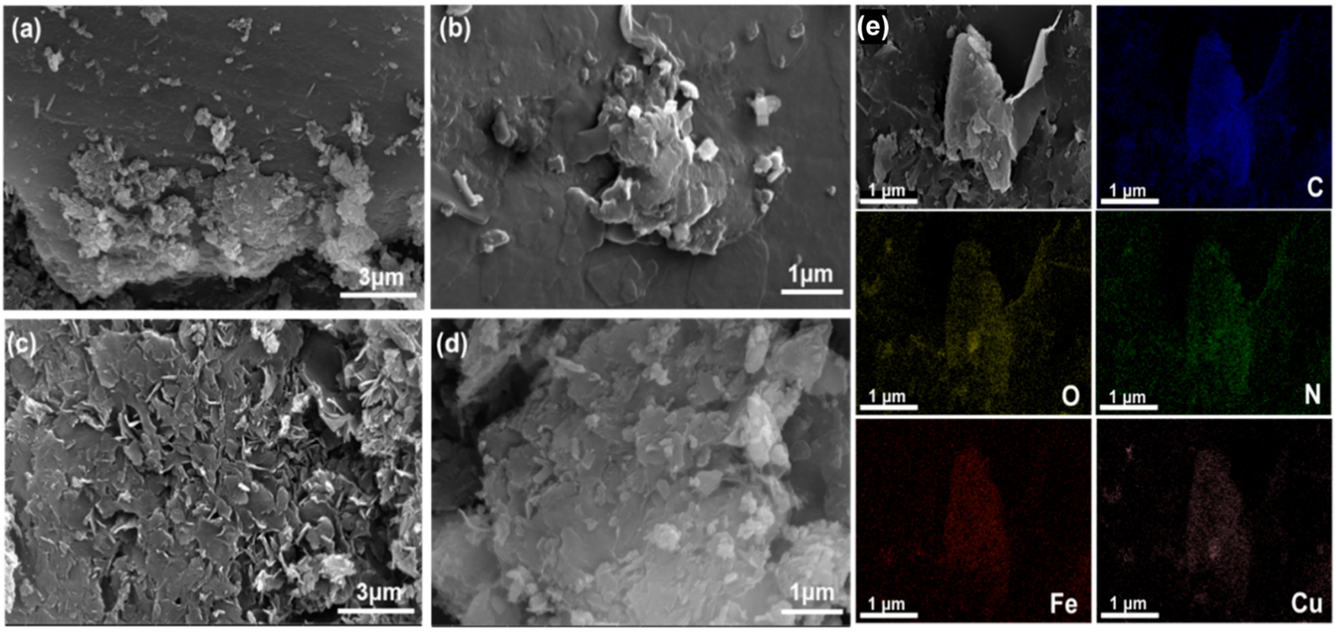

Figure 2. SEM images of (a,b) hemin/rGO, (c,d) Cu-hemin MOF/rGO nanocomposites; EDS spectrum and C, N, O, Fe, and Cu elemental mapping of (e) Cu-hemin MOF/rGO material.

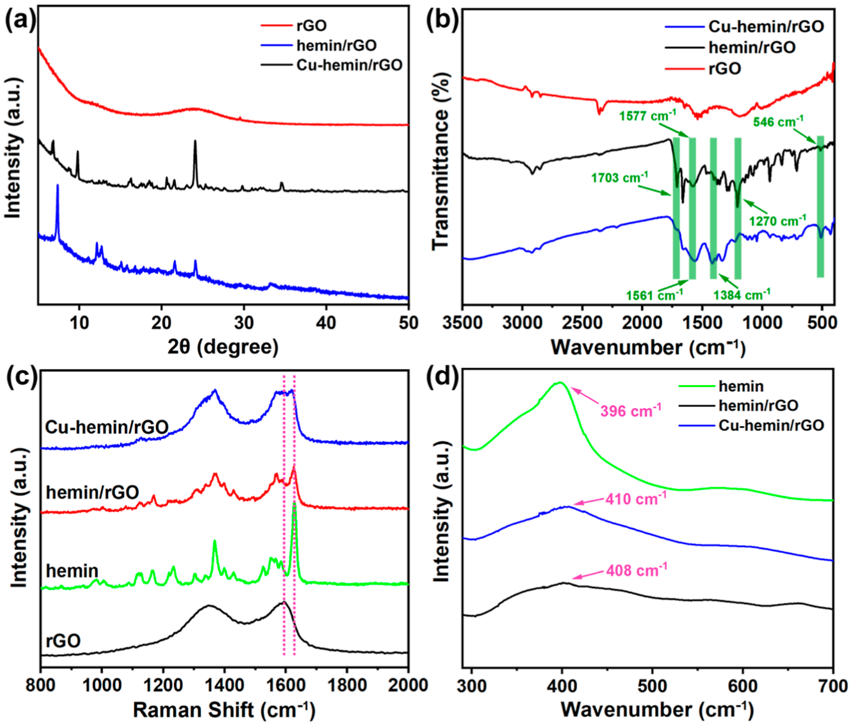

Figure 3. (a) Powder XRD patterns of rGO, hemin/rGO, and Cu-hemin MOF/rGO. (b) FT-IR spectra of rGO, hemin/rGO, and Cu-hemin MOF/rGO. (c) Raman spectra of rGO, hemin/rGO, and Cu-hemin MOF/rGO. (d) UV−vis spectra of pure hemin, hemin/rGO, and Cu-hemin MOF/rGO.

peak undergoes a red shift. These results suggest that Cu-hemin interacts closely via $\pi-\pi$ stacking with the conjugated aromatic framework of rGO, which consequently reduces the distance between Cu-hemin and rGO.[49] In both the Cu-hemin MOF/rGO and hemin/rGO samples, a characteristic broad, blunt, and weak absorption peak is observed at around 3300 cm^{-1}. This peak corresponds to the associated hydroxyl group in hemin.[50] The absorption peak at 1625 cm^{-1} can be ascribed to the stretching vibration of the −C═N bond on the porphyrin ring. Meanwhile, the weak signal peak at 546 cm^{-1} is associated with the Fe−N bond. These observations suggest the successful incorporation of hemin molecules.[51] The difference is that due to the coordination of Cu^{2+} and −COOH groups, the strong stretching vibration of carbonyl functional group C═O in Cu-hemin MOF/rGO is shifted from 1703 to 1690 cm^{-1} compared with hemin/rGO, and the peak strength is also greatly weakened. In addition, the intensity of the C−OH stretching vibration peak at 1270 cm^{-1}

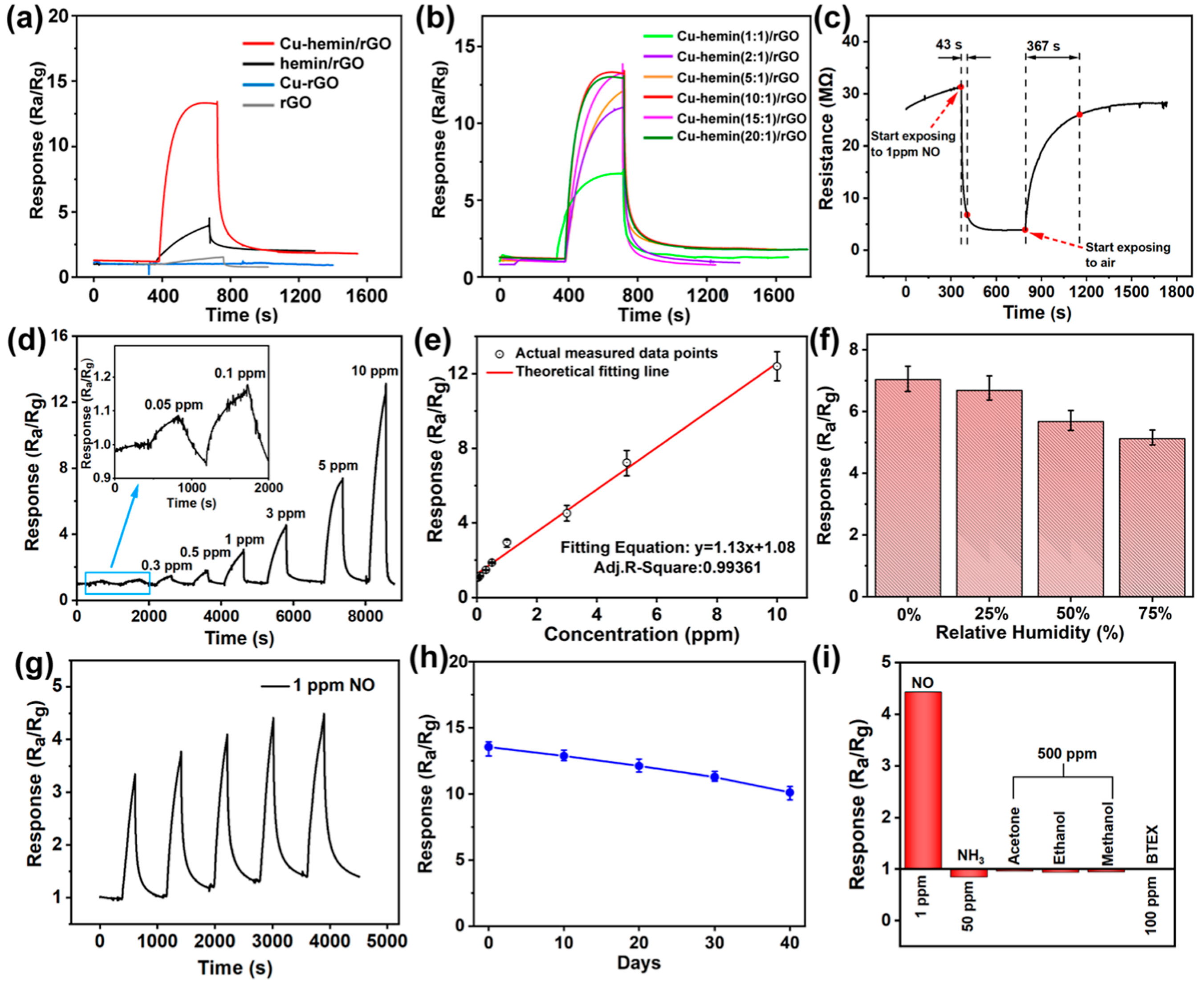

Figure 4. Typical response curve (a) after 10 ppm of NO exposure at pristine rGO, Cu-hemin MOF, hemin/rGO, and Cu-hemin MOF/rGO; (b) response curves of Cu-hemin MOF/rGO materials with different molar ratios under 10 ppm of NO; (c) response and recovery time of the Cu-hemin MOF/rGO toward 10 ppm of NO; response curves of (d) Cu-hemin MOF/rGO-based sensors to NO at concentrations varying from 0.05 to 10 ppm and (e) corresponding fitted curve of the response; response (f) of the sensor toward 5 ppm of NO at different RH values ranging from 0% to 75% at RT; (g) five cyclic response curves of the Cu-hemin MOF/rGO sensor toward 1 ppm of NO; (h) aging test of Cu-hemin MOF/rGO sensors toward 10 ppm of NO for 40 days; and selectivity (i) of the sensor to various exhaled interfering gases at much higher concentrations. The same sensors were tested 3 times to obtain the response values and error bars.

in the Cu-hemin MOF/rGO spectrum also decreased.[42,44,52] The peak at 1384 cm^{-1} is indicative of the $-CH_3$ bending vibration. This peak appears more prominent in the spectrum of the Cu-hemin MOF, presumably because of the ordered assembly of hemin within the Cu-hemin MOFs.[41] Therefore, the FT-IR spectra also serve as evidence for the formation of Cu-hemin MOFs and the successful assembly of the hemin-MOF with the rGO.

The Raman spectra of rGO displayed the characteristic features typical of graphene-based materials (Figure 3c). After one-step solvothermal treatment, three characteristic sharp peaks of hemin at 1360, 1560, and 1610 cm^{-1} remained in the Raman spectra of hemin/rGO and Cu-hemin MOF/rGO, confirming the successful attachment of Fe-porphyrin rings to the graphene after they were rinsed several times rinsing by DMF, anhydrous ethanol, and DI water, respectively.[53] Figure 3d shows the UV−vis absorption spectra of hemin, hemin/rGO, and Cu-hemin MOF/rGO. The absorption peaks all appeared at around 400 nm (Soret peak), which indicates that the Fe-porphyrin rings remained intact throughout the solvothermal process, ensuring their capacity to interact with NO molecules. However, a slight red-shift occurred in the absorption peak of hemin/rGO and Cu-hemin MOF/rGO with a broader absorption around 410 nm. This red-shift is primarily caused by the $\pi-\pi$ interaction between rGO and hemin. This interaction rotates the ethylene groups to a coplanar conformation with the porphyrin ring and flattens the hemin molecule, thereby enhancing the π conjugation.[48,54]

The XPS spectrum of Cu-hemin MOF/rGO showed the material containing Cu, Fe, C, N, and O peaks obviously, which was similar to the previous Cu-hemin MOF materials (Figure S2),[43,47] also indicating the successful synthesis of Cu-hemin MOF; the XPS spectra of Cu 2p exhibited four peaks at the following binding energies: 934.5, 942.1, 943.8, and 954.3

eV. The peaks at 934.5 and 954.3 eV correspond to Cu $2p_{1/2}$ and Cu $2p_{3/2}$, while the peaks of 942.1 and 943.8 eV were identified as satellite peaks of Cu^{2+}, proving that the copper element existed as divalent cations. The Fe 2p XPS spectrum (Figure S2c) showed two characteristic peaks corresponding to Fe $2p_{1/2}$ and Fe $2p_{3/2}$.[43] All these results indicate the successful synthesis of Cu-hemin MOF.

3.2. NO Sensing Properties. To investigate the gas sensing properties, the as-prepared samples were used as sensing materials to fabricate sensors on IDEs. The details are provided in the Experimental Section. The excellent nitric oxide sensing properties of the Cu-hemin MOF/rGO offer a theoretical basis for the fabrication of high-performance gas sensors. Figure 4a shows typical gas response/recovery curves of the Cu-hemin MOF, rGO, hemin/rGO, and Cu-hemin MOF/rGO toward 10 ppm of NO. As shown in Figure 4a, the sample that contained only Cu-hemin MOF had minimal electrical conductivity and demonstrated almost negligible gas response to NO. Meanwhile, the pure rGO and hemin/rGO also exhibited much weaker NO sensing performance, as reported in our previous work compared to the Cu-hemin MOF/rGO sample.[10]

The superior gas sensing performance of Cu-hemin MOF/rGO may result from the disruption of hemin crystallization due to the coordination of Cu^{2+} with the carboxyl group in the hemin molecule. More details will be discussed in the Gas Sensing Mechanism part. A series of Cu-hemin MOF/rGO with different molar ratios of metal ions and hemin were prepared and named Cu-hemin MOF(x:1)/rGO. All these control groups had the sensing test toward 10 ppm of NO. From Figure 4b, we can see that when Cu^{2+} was added to the system, the sensor's response enhanced significantly with the increase of the Cu^{2+} ratio, and when the feeding ratio is greater than 10:1, the performance of Cu-hemin MOF/rGO sensors stabilizes, which may be because ethanol solvent has less polarity than water and a reduced solubility for $Cu(NO_3)_2$, so the amount of Cu-hemin MOF produced beyond a certain upper limit reached saturation. Therefore, Cu-hemin MOF(10:1)/rGO was used in the following NO sensing test.

According to the UV characterization spectra in Figure S4a, a certain amount of hemin molecules remained in the samples that were either not cleaned or cleaned only once, while the samples that were cleaned five times could be considered to contain almost no remaining hemin molecules. To confirm whether the residual hemin molecules in the Cu-hemin MOF/rGO system affect the NO gas-sensitive performance, we conducted gas sensitivity tests using different Cu-hemin MOF/rGO sensors with varying cleaning times under the same conditions and maintaining a test concentration of NO at 10 ppm. The response results are shown in Figure S4b. Based on the response results to NO, the Cu-hemin MOF/rGO sensors showed basically the same response after different cleaning times, indicating that the enhanced response performance to NO was due to the contribution of Cu-hemin MOF on graphene rather than the involvement of residual hemin molecules. As shown in Figure 4c, the Cu-hemin MOF/rGO exhibited a relatively swift response and recovery to 10 ppm of NO with a τ_{res} of 43 s and a τ_{rec} of 367 s. The fast response speed is attributed to the decrease of accumulation of hemin and Cu-hemin MOF's higher surface area and porous structure.

Figure 4d shows the continuous dynamics-sensing response of Cu-hemin MOF/rGO toward NO with concentrations ranging from 0.05 to 10 ppm. It is clear that with the increase in the NO concentration, the response of the sensor increased from 1.06 to 13.4; especially, there is an obvious response peak that can be seen even at a low concentration of 50 ppb (inset of Figure 4d), which exhibits a very competitive NO sensitivity. The response values also exhibited good linearity to various NO concentrations with a regression coefficient (R^2) of 0.99361, which is significant for practical applications (Figure 4e). It is clear that the Cu-hemin MOF/rGO sensor exhibits extremely sensitive performance to NO, attributed to the special interaction between the Cu-hemin MOF/rGO and NO molecules.

To further illustrate the excellent selectivity of the sensor when detecting multiple exhaled gases, another experiment was carried out. In this experiment, one of the five interfering gases was injected together with NO. We kept the NO maintaining at 1 ppm, and NH_3 was injected to achieve 50 ppm, while the others were injected to reach 500 ppm. Although the concentration of the interfering gases was 1−10 orders of magnitude higher than that of NO, the response of the Cu-hemin MOF/rGO to NO remained relatively stable at approximately 90%, with only slight fluctuations (Figure S3). This indicates that our sensor can accurately identify and measure the concentration of NO gas and is relatively unaffected by the presence of other interfering gas biomarkers.

Additionally, different levels of RH ranging from 0% to 70% were selected to investigate the humidity effects on the material's sensing performance toward 5 ppm of NO, and the corresponding curves are drawn in Figure 4f. In contrast to dry conditions, the sensors exhibited a modest decrease in response upon exposure to NO with the increase of RH. The decline in response may result from the competition between the water molecules and NO molecules, both of which could come in contact with the Fe^{3+} ion of the Fe−N_4 moiety. Although the Cu-hemin MOF/rGO sensor's humidity resistance is better than some previous NO sensors, its properties are still under the effect of humidity interference. With the help of the gas-drying technology, this problem could be solved, analogous to what has been achieved in contemporary exhaled breath detection.[55]

Furthermore, it is important for sensors to exhibit repeatability and recoverability for practical applications. Here, in Figure 4g, a five-response/recovery cycle curve of the Cu-hemin MOF/rGO toward 1 ppm of NO, which was obtained. The average response was 2.86, and there are little differences of response in each NO-sensing cycle, revealing its great repeatability and recoverability.

An aging stability test of the Cu-hemin MOF/rGO sensor device was conducted over a period of more than 40 days to demonstrate that the material has a long service life to meet the requirements of practical applications (Figure 4h). The prepared device maintained a high response (less than 20% decrease) to 10 ppm of NO over the entire testing period, suggesting its relatively reliable long-term stability. We also conducted a long-term stability test of the material dispersion. Every 60 days, we prepared a new sensor, whose materials come from the same material dispersion. As shown in Figure S5, after 360 days, the synthetic material dispersion still can prepare a new sensor with outstanding sensing performance.

Meanwhile, it is well-known that gas sensors must have the ability to distinguish the target gas from other interfering components and avoid the effects of humidity especially in exhaled breath testing. Figure 4i displays the different sensing

Table 1. Summary of the NO Gas Sensing Performance of Carbon-Based Materials at RT[a]

materials	concentration (ppm)	response	τ_{res}/τ_{rec} (s/s)	stability (days)	pLOD (ppm)	reference
TiO_2@NGQDs	10	0.95	235/285		10	56
MoS_2/rGO/paper	2	1.06	150/>600		2	57
CNFs/CoS_2/MoS_2	1	~0.9	1200/6000		1	58
en-APTAS@SWCNTs	0.1	1.25	~600/>600	35	0.1	59
TiO_2/rGO	2.75	1.06	440/811		0.7	60
SWCNT@PEI	1	2.5	~1800 > 3000		0.1	61
WS_2/MWCNT	1		285/198 (0.01 ppm)	42	0.001	62
PBDTTT-C-T(UV-enhanced)	1	2.4	50/120		0.01	63
hemin-N-rGO	1	1.34	229/770	30	0.5	10
HNS-rGO	1	1.6	145/423	30	0.1	27
Cu-hemin MOF/rGO (*this work*)	**1**	**3.42**	**43/367**	**40**	**0.05**	***this work***

[a] Response time (τ_{res}), recovery time (τ_{rec}), pLOD, and studied detection range (D_R). Stability refers to the long-term stability. For the convenience of comparison, the response is denoted as response = R_a/R_g.

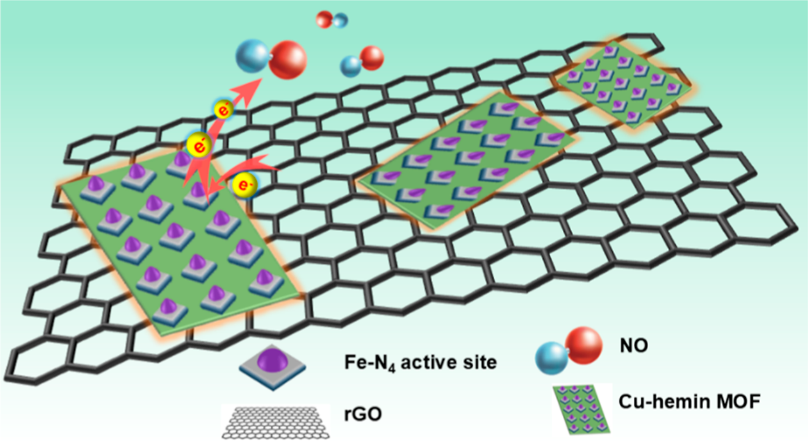

Figure 5. Schematic illustration of the enhanced sensing mechanism on Cu-hemin MOF/rGO nanocomposites.

results of the Cu-hemin MOF/rGO to the corresponding exhaled gases. The Cu-hemin MOF/rGO sensor showed a much higher response toward NO (R_a/R_g = 2.96, 1 ppm) than other exhaled gases including ammonia (R_g/R_a = 0.93, 50 ppm), acetone (R_g/R_a = 0.89, 500 ppm), ethanol (R_g/R_a = 0.96, 500 ppm), methanol (R_g/R_a = 0.98, 500 ppm), and benzene, toluene, ethylbenzene, and xylene (BTEX) (R_g/R_a = 1, 100 ppm).

The performance of the Cu-hemin MOF/rGO sensor significantly surpasses the existing typical room-temperature NO sensors reported in the literature, as summarized in Table 1. It should be noted that the pLOD of 50 ppb was a highlight among these NO sensors. Furthermore, the Cu-hemin MOF/rGO sensor is characterized by a relatively short response/recovery time and remarkable long-term stability. Consequently, the exceptional NO sensing capabilities of the Cu-hemin MOF/rGO render it a highly promising candidate for room-temperature NO sensors. Additionally, we observed that the reaction time and recovery time vary for different materials. This should be due to the differences in the affinity of the reaction sites for NO, leading to variations in both response and recovery times. In the Cu-hemin MOF/rGO composite we reported, the Fe−N_4 sites exhibit a strong affinity toward NO, which results in a faster response time. However, during desorption, the strong affinity between NO and Fe−N_4 sites slows the NO desorption speed, leading to a longer recovery time.

To confirm the role of the self-assembly process on NO detection performance, we compared the response of the composite materials obtained through physical mixing and self-assembly to 1 ppm of NO. As shown in Figure S8, it was observed that the physically mixed composite material showed a lower response to NO, which can be attributed to the limited response of rGO to NO, while the self-assembled composite material exhibited a significant response to NO. This comparison clearly demonstrates that the self-assembly process plays a decisive role in the high-sensitivity detection of NO.

3.3. Gas Sensing Mechanism.

It is well-known that phthalocyanine and porphyrin compounds with coordinating metal cations, especially Fe(III), in their centers can interact with NO molecules in solution. According to the DFT calculation results reported in previous studies,[32,64,65] the binding of NO to Fe-porphyrin triggers a substantial alteration in the electronic structures of Fe-porphyrin, namely, the charge transfer from the Fe-porphyrin to NO molecules. Hence, in this case, for the hemin/rGO and Cu-hemin MOF/rGO nanocomposites, the sensing process can be described as follows: (1) first NO molecules are adsorbed onto the porphyrin ring of hemin to interact with Fe(III). (2) Under the interaction of the NO molecule, a significant change in the electronic structures of Fe-porphyrin has occurred, specifically, the charge transfer between the NO molecule and Fe-porphyrin, and NO gain the electron. (3) Due to the strong electronegativity of NO, a large number of electrons are transferred from graphene to the Fe-porphyrin (Figure 5).[10,48]

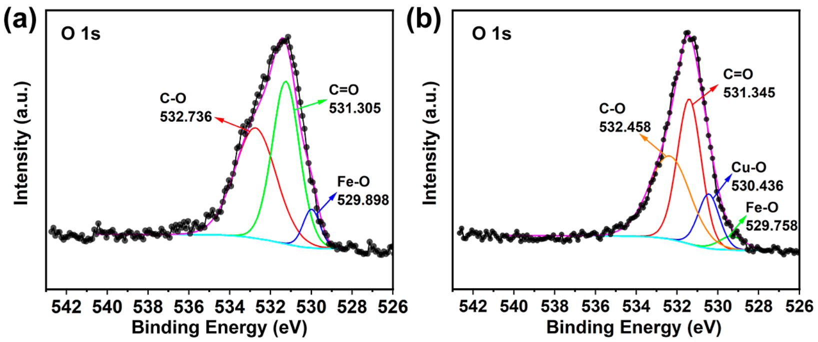

Figure 6. XPS O 1s spectra of hemin/rGO (a) and Cu-hemin MOF/rGO (b).

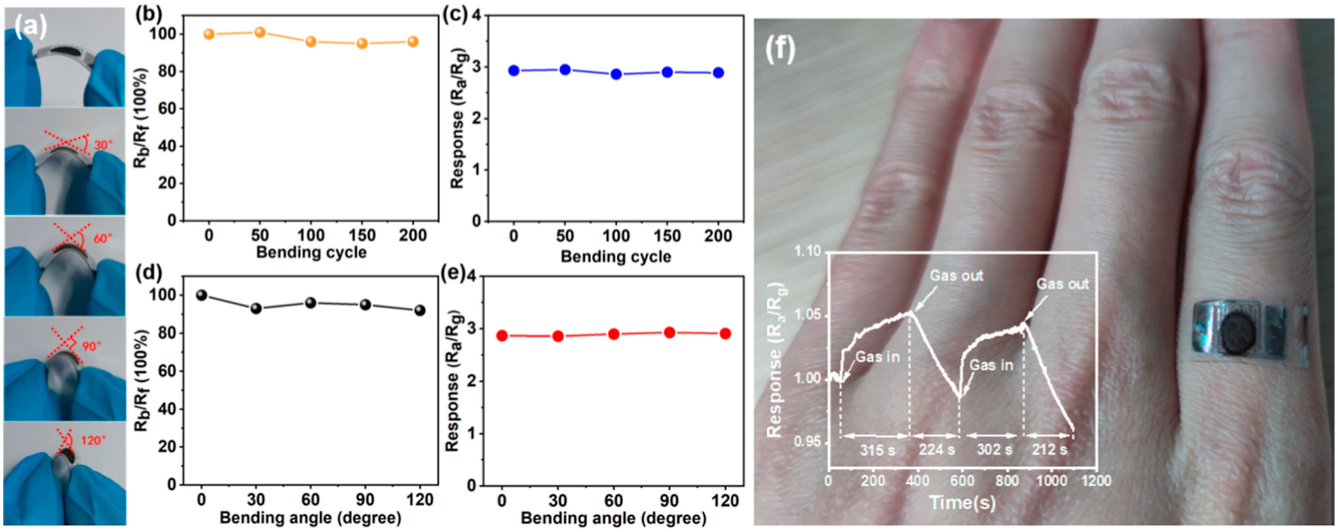

Figure 7. (a) Photograph of the sensing device with different bending angles. (b,c) Stability test of the device in different atmospheres. (d,e) Bending test under different atmospheres with various bending angles. (f) Fully flexible sensor highly conformably attached to a bent human hand (the upper right inset is responsivity for the skin sensor at 50 ppb NO gas).

The efficient electron transport via the $\pi-\pi$ interaction between rGO and Fe-porphyrin boosts the quantity of holes on the p-type graphene nanosheets. This, in turn, results in a reduction of the resistance of the sensing material.[54]

Here comes another question: why do the Cu-hemin MOF/rGO nanocomposites show a much better sensing response than the hemin/rGO. To investigate this question, the high-resolution XPS spectra of O 1s of two sensing materials were obtained and are shown in Figure 6. For hemin/rGO, there are two carboxyl groups containing hemin molecules, and previous research shows that hemin aggregates are very inclined to form hydrogen-bonded head-to-tail dimers, where the central iron ion in the porphyrin ring of one hemin molecule tends to coordinate with a carboxylate oxygen of another hemin molecule. This behavior will lead to a decline of Fe(III)$-N_4$ active sites. As shown in Figure 6a, three peaks centered at 532.736, 531.305, and 529.898 eV were attributed to C$-$O, C$=$O, and Fe$-$O bonds, respectively.[10,66] The existence of the Fe$-$O bond peak confirms that numerous central iron ions of Fe-porphyrin have been occupied in hemin/rGO, resulting in an inferior performance toward NO.[10] By contrast, in O 1s of Cu-hemin MOF/rGO (Figure 6b), a new peak corresponding to Cu$-$O was found at 530.436 eV, while the intensity of the peak on behalf of the Fe$-$O bond around 529.758 eV was much weaker.[67,68] Because of the coordination with Cu^{2+}, fewer carboxylate oxygens of hemin can contact the central Fe(III) of the adjacent hemin molecule, thus releasing more Fe(III)$-N_4$ active sites to interact with NO, making Cu-hemin MOF/rGO sensors exhibit a more sensitive performance toward NO. In addition, the Cu-hemin MOF's higher specific surface area and porous structure are also beneficial for NO gas adsorption.

To further investigate the mechanism of performance enhancement of Cu-hemin MOF/rGO, control groups were obtained by replacing Cu^{2+} with other excessive metal divalent cations such as Zn^{2+} and Ni^{2+}, and the corresponding products were named Zn-hemin/rGO and Ni-hemin/rGO. Figure S6 shows the result of these three materials' sensing to 10 ppm of NO at RT, respectively. It is obvious that three samples got nearly the same responses, indicating that the Cu^{2+} here only acted as a bridge to link hemin molecules and consume the free carboxyl of hemin; it is not important to replace the Cu^{2+} with other metal ions as long as it can coordinate with a carboxyl group.

In summary, the enhancement of the NO sensing performance could be concluded into a decline of the formation of Fe$-$O bond and an increase in the number of the Fe(III)$-N_4$ active sites to interact with NO.

3.4. Wearability Test of the Gas Sensor. To achieve the wearability of the device, it is inevitable that the sensor should possess the characteristics of being lightweight, thin, flexible, and mechanically stable. Flexible NO sensors made from the

Cu-hemin MOF/rGO material were prepared on the PET and PDMS substrate; Figure 7a demonstrates that the sensing device was bent at various bending angles including 30, 60, 90°, and 120°. As shown in Figure 7, the resistance retention (R_b/R_f, where R_b and R_f denote the resistance of the sensing device under flat and bending conditions, respectively) showed a minor decrease in both air and NO gas (1 ppm) environments, saying that the sensor's electrical properties and sensing performances do not change much under bending (Figure 7b,c). Additionally, the sensing device was capable of withstanding 200 times bending, where the angle was 120° each time. Moreover, the resistance retention remained at its original value under both air conditions (Figure 7d) and in the presence of 1 ppm of NO gas (Figure 7e). These observations indicate that the flexible Cu-hemin MOF/rGO sensor has high flexibility and mechanical strength while maintaining an excellent NO sensing performance. Additionally, a fully flexible sensor that can fit tightly to the skin was prepared on a PDMS substrate by Magnetron sputtering. The device is semi-transparent and exhibits skin-like conformability, which allows for the creation of a skin-like device (Figure 7f). Finally, our flexible sensor can still have responsivity toward 50 ppb of NO gas and the response were up to 3%, making it suitable for wearable electronic device arrays.

4. CONCLUSIONS

In summary, by designing a sheet-on-sheet structure, we have successfully prepared a sensitive, fast RT nitric oxide sensor based on Cu-hemin MOF/rGO nanocomposites by a simple solvothermal method. The Cu-hemin MOF possesses a nanometer-scale structure, which contributes to its high surface area and enhanced interaction with target molecules. The Cu-hemin MOF/rGO exhibits 5.1-fold higher response to NO sensing at RT compared to that of the pristine material hemin/rGO, with reliable repeatability, relatively short response/recovery time (43 s/367 s), good selectivity (1.13), and long-term stability (360 days). Even more notably, the sensor achieved a remarkably low pLOD of 50 ppb toward NO at RT, showing great potential in exhale diagnosis. We hypothesized that the excellent NO gas-sensing properties were primarily due to the greater number of Fe(III) active sites in Fe-porphyrin. These active sites were generated as a result of the formation of Cu-hemin MOF through the coordination between Cu^{2+} and the carboxyl group of hemins. The results of this study indicated the potential of the sensor for the early detection of airway inflammatory disease. Furthermore, a fully flexible device based on the Cu-hemin MOF/rGO nanocomposite sensor was fabricated to guarantee the ease of wearing and carrying gas sensors, thereby paving the way for the next-generation wearable intelligent electronics.

■ ASSOCIATED CONTENT

Supporting Information

The Supporting Information is available free of charge at https://pubs.acs.org/doi/10.1021/acsanm.4c06397.

> Flowchart of flexible electrode preparation, XPS spectra of Cu-hemin/rGO and high resolution spectra of Cu 2p and Fe 2p, sensing performance of the device when simultaneously exposed to 1 ppm of NO and another exhaled interfering gases at various concentrations, UV—vis of pure hemin and the filtrates for different orders and the performances toward 10 ppm of NO of samples that have been washed at different times, long-term sensing performance stability test of Cu-hemin MOF/rGO material dispersion, responses toward 10 ppm of NO of metal-hemin derivatives with different metal ion introducing, responses toward 10 ppm of NO of Cu-hemin MOF/rGO prepared in different solvent, response of Cu-hemin MOF/rGO to 10 ppm of NO_2 and NO, comparison of the response of physical hybrid composites with Cu-hemin/rGO to 1 ppm of NO (PDF)

■ AUTHOR INFORMATION

Corresponding Author

Yao Wang − *Guangdong Provincial Key Laboratory of Optical Information Materials and Technology, Institute of Electronic Paper Displays, South China Academy of Advanced Optoelectronics, South China Normal University, Guangzhou 510006, P. R. China; National Center for International Research on Green Optoelectronics, South China Normal University, Guangzhou 510006, P. R. China;* orcid.org/0000-0002-0713-5018; Email: wangyao@m.scnu.edu.cn

Authors

You Wu − *Guangdong Provincial Key Laboratory of Optical Information Materials and Technology, Institute of Electronic Paper Displays, South China Academy of Advanced Optoelectronics, South China Normal University, Guangzhou 510006, P. R. China; National Center for International Research on Green Optoelectronics, South China Normal University, Guangzhou 510006, P. R. China*

Weiran Li − *Guangdong Provincial Key Laboratory of Optical Information Materials and Technology, Institute of Electronic Paper Displays, South China Academy of Advanced Optoelectronics, South China Normal University, Guangzhou 510006, P. R. China; National Center for International Research on Green Optoelectronics, South China Normal University, Guangzhou 510006, P. R. China*

Yanwei Chang − *Guangdong Provincial Key Laboratory of Optical Information Materials and Technology, Institute of Electronic Paper Displays, South China Academy of Advanced Optoelectronics, South China Normal University, Guangzhou 510006, P. R. China; National Center for International Research on Green Optoelectronics, South China Normal University, Guangzhou 510006, P. R. China*

Yixun Gao − *Guangdong Provincial Key Laboratory of Optical Information Materials and Technology, Institute of Electronic Paper Displays, South China Academy of Advanced Optoelectronics, South China Normal University, Guangzhou 510006, P. R. China; National Center for International Research on Green Optoelectronics, South China Normal University, Guangzhou 510006, P. R. China;* orcid.org/0000-0001-8617-472X

Fengnan Wang − *Department of Thoracic Oncology, State Key Laboratory of Respiratory Diseases, The First Affiliated Hospital of Guangzhou Medical University, Guangzhou 510006, P. R. China*

Hao Li − *Guangdong Provincial Key Laboratory of Optical Information Materials and Technology, Institute of Electronic Paper Displays, South China Academy of Advanced Optoelectronics, South China Normal University, Guangzhou 510006, P. R. China; National Center for International Research on Green Optoelectronics, South China Normal University, Guangzhou 510006, P. R. China*

Paddy J. French − *BE Laboratory, EWI, Delft University of Technology, Delft 2628CD, The Netherlands*

Yi-Kuen Lee − *Department of Mechanical & Aerospace Engineering, Hong Kong University of Science and Technology, Kowloon 999077 Hong Kong Special Administrative Region, Hong Kong; Department of Electronic & Computer Engineering, Hong Kong University of Science and Technology, Kowloon 999077 Hong Kong Special Administrative Region, Hong Kong*

Sheikh A. Akbar − *Department of Materials Science and Engineering, The Ohio State University, Columbus, Ohio 43055, The United States;* orcid.org/0000-0003-3567-274X

Ahmad M. Umar Siddiqui − *Department of Chemistry, Faculty of Science and Arts and Promising Centre for Sensors and Electronic Devices (PCSED), Najran University, Najran 11001, Saudi Arabia*

Guofu Zhou − *Guangdong Provincial Key Laboratory of Optical Information Materials and Technology, Institute of Electronic Paper Displays, South China Academy of Advanced Optoelectronics, South China Normal University, Guangzhou 510006, P. R. China;* orcid.org/0000-0003-1101-1947

Complete contact information is available at:
https://pubs.acs.org/10.1021/acsanm.4c06397

Author Contributions

You Wu and Weiran Li: Writing—review and editing, writing—original draft, visualization, methodology, investigation, formal analysis, data curation, and conceptualization. **Yanwei Chang**: Writing—review and editing. **Yixun Gao**: Validation and funding acquisition. **Fengnan Wang**: Conceptualization. **Hao Li**: Conceptualization. **Paddy J. French**: Conceptualization. **Yi-Kuen Lee**: Conceptualization. **Sheikh A. Akbar**: Conceptualization. **Ahmad M. Umar Siddiqui**: Conceptualization. **Guofu Zhou**: Conceptualization. **Yao Wang**: Writing—review and editing, validation, supervision, resources, funding acquisition, and conceptualization.

Notes

The authors declare no competing financial interest.

■ ACKNOWLEDGMENTS

This work was supported by National Natural Science Foundation of China (grant no.51973070), Guangdong Basic and Applied Basic Research Foundation (no.2025A1515012116), Department of Science and Technology of Guangxi Province (no. AB25069461), Startup Foundation from SCNU, Guangdong Provincial Key Laboratory of Optical Information Materials and Technology (2023B1212060065), and the 111 Project.

■ REFERENCES

(1) Wei, X.; Tian, J.; Wang, C.; Cheng, S.; Fei, X.; Yin, F.; Xu, L.; Li, Y. A soft electronic skin simulating the multi-scale human touch for the detection of fruit freshness. *J. Colloid Interface Sci.* **2025**, *680*, 66−76.

(2) Tang, C.; Li, Y.; Fei, X.; Zhao, W.; Tian, J.; Xu, L.; Wang, Y. An integrally formed Janus supramolecular bio-gel with intelligent adhesion for multifunctional healthcare. *J. Colloid Interface Sci.* **2025**, *680*, 1030−1041.

(3) Davenport, A. J.; Cross, R.; Watson, K.; Liao, Y.; Shi, W.; Prince, H.; Beavis, P.; Trapani, J.; Kershaw, M.; Ritchie, D.; Darcy, P.; Neeson, P.; Jenkins, M. Chimeric antigen receptor T cells form nonclassical and potent immune synapses driving rapid cytotoxicity. *Proc. Natl. Acad. Sci. U.S.A.* **2018**, *115* (9), E2068−E2076.

(4) Dweik, R.; Boggs, P.; Erzurum, S.; Irvin, C.; Leigh, M.; Lundberg, J.; Olin, A.; Plummer, A.; Taylor, D. An Official ATS Clinical Practice Guideline: Interpretation of Exhaled Nitric Oxide Levels (FENO) for Clinical Applications. *Proc. Natl. Acad. Sci. U.S.A.* **2011**, *184*, 602−615.

(5) Nagano, T.; Yoshimura, T. Bioimaging of Nitric Oxide. *Chem. Rev.* **2002**, *102* (4), 1235−1269.

(6) Ratnawati, M.; Morton, J.; Henry, R.; Thomas, P. Exhaled breath condensate nitrite/nitrate and pH in relation to pediatric asthma control and exhaled nitric oxide. *Pediatr. Pulmonol.* **2006**, *41* (10), 929−936.

(7) Zacharasiewicz, A.; Wilson, N.; Lex, C.; Erin, E. M.; Li, A. M.; Hansel, T.; Khan, M.; Bush, A. Clinical use of noninvasive measurements of airway inflammation in steroid reduction in children. *Am. J. Respir. Crit. Care Med.* **2005**, *171* (10), 1077−1082.

(8) American Thoracic Society Workshop. ATS Workshop Proceedings: Exhaled nitric oxide and nitric oxide oxidative metabolism in exhaled breath condensate: Executive summary. *Am. J. Respir. Crit. Care Med.* **2006**, *173* (7), 811−813.

(9) Lee, D.; Yun, M. J.; Kim, K. H.; Kim, S.; Kim, H. D. Advanced Recovery and High-Sensitive Properties of Memristor-Based Gas Sensor Devices Operated at Room Temperature. *ACS Sens.* **2021**, *6* (11), 4217−4224.

(10) Gao, Y.; Wang, J.; Feng, Y.; Cao, N.; Li, H.; De Rooij, N.; Umar, A.; French, P.; Wang, Y.; Zhou, G. Carbon-Iron Electron Transport Channels in Porphyrin-Graphene Complex for ppb-Level Room Temperature NO Gas Sensing. *Small* **2022**, *18* (11), 2103259.

(11) Kleschyov, A.; Wenzel, P.; Munzel, T. Electron paramagnetic resonance (EPR) spin trapping of biological nitric oxide. *J. Chromatogr. B:Anal. Technol. Biomed. Life Sci.* **2007**, *851* (1−2), 12−20.

(12) Kipping, P.; Jeffery, P. Detection of Nitric Oxide by Gas-chromatography. *Nature* **1963**, *200* (NO), 1314.

(13) Zhou, Y.; Gu, Q.; Qiu, T.; He, X.; Chen, J.; Qi, R.; Huang, R.; Zheng, T.; Tian, Y. Ultrasensitive Sensing of Volatile Organic Compounds Using a Cu-Doped SnO_2-NiO p-n Heterostructure That Shows Significant Raman Enhancement. *Angew. Chem., Int. Ed.* **2021**, *60* (50), 26260−26267.

(14) Kim, M.; Naveen, M.; Gurudatt, N.; Shim, Y. Detection of Nitric Oxide from Living Cells Using Polymeric Zinc Organic Framework-Derived Zinc Oxide Composite with Conducting Polymer. *Small* **2017**, *13* (26), 1700502.

(15) Li, C.; Song, B.; Lv, M.; Chen, G.; Zhang, X.; Deng, Z.; Xu, Y.; Huo, L.; Gao, S. Highly sensitive and selective nitric oxide sensor based on biomorphic ZnO microtubes with dual-defects assistance at low temperature. *Chem. Eng. J.* **2022**, *446*, 136846.

(16) Tammanoon, N.; Iwamoto, T.; Ueda, T.; Hyodo, T.; Wisitsoraat, A.; Liewhiran, C.; Shimizu, Y. Synergistic Effects of PdO_x−CuO_x Loadings on Methyl Mercaptan Sensing of Porous WO_3 Microspheres Prepared by Ultrasonic Spray Pyrolysis. *ACS Appl. Mater. Interfaces* **2020**, *12* (37), 41728−41739.

(17) Ma, Z.; Yang, K.; Xiao, C.; Jia, L. Electrospun Bi-doped SnO_2 porous nanosheets for highly sensitive nitric oxide detection. *J. Hazard. Mater.* **2021**, *416*, 126118−126128.

(18) Yang, D.; Gopal, R.; Lkhagvaa, T.; Choi, D. Metal-Oxide Gas Sensors for Exhaled-Breath Analysis: A Review. *Meas. Sci. Technol.* **2021**, *32* (10), 102004−102023.

(19) Barsan, N.; Simion, C.; Heine, T.; Pokhrel, S.; Weimar, U. Modeling of Sensing and Transduction for p-type Semiconducting Metal Oxide Based Gas Sensors. *J. Electroceramics* **2010**, *25* (1), 11−19.

(20) Naderi, H.; Hajati, S.; Ghaedi, M.; Espinos, J. Highly Selective Few-ppm NO Gas-Sensing Based on Necklace-Like Nanofibers of ZnO/CdO n-n Type Heterojunction. *Sens. Actuators, B* **2019**, *297*, 126774.

(21) Ri, Y.; Kim, S.; Kye, Y.; Jong, Y.; Kang, M.; Yu, C. First-principles study of molecular hydrogen binding to heme in

competition with O_2, NO and CO. *RSC Adv.* **2024**, *14* (24), 16629−16638.

(22) Klyamer, D.; Bonegardt, D.; Basova, T. Fluoro-Substituted Metal Phthalocyanines for Active Layers of Chemical Sensors. *Chemosensors* **2021**, *9* (6), 133.

(23) Giancane, G.; Valli, L. State of Art in Porphyrin Langmuir−Blodgett Films as Chemical Sensors. *Adv. Colloid Interface Sci.* **2012**, *171−172*, 17−35.

(24) Sarkar, A.; Carter, E. L.; Harland, J. B.; Speelman, A. L.; Lehnert, N.; Ragsdale, S. W. Ferric heme as a CO/NO sensor in the nuclear receptor Rev-Erbß by coupling gas binding to electron transfer. *Proc. Natl. Acad. Sci. U.S.A.* **2021**, *118* (3), No. e2016717118.

(25) Lehnert, N.; Kim, E.; Dong, H.; Harland, J.; Hunt, A.; Manickas, E.; Oakley, K.; Pham, J.; Reed, G.; Alfaro, V. The Biologically Relevant Coordination Chemistry of Iron and Nitric Oxide: Electronic Structure and Reactivity. *Chem. Rev.* **2021**, *121* (24), 14682−14905.

(26) Zhang, C.; Hu, F.; Hao, X.; Rao, Q.; Hu, T.; Sun, W.; Guo, C.; Li, C. Sandwiching Phosphorene with Iron Porphyrin Monolayer for High Stability and Its Biomimetic Sensor to Sensitively Detect Living Cell Released NO. *Adv. Sci.* **2022**, *9* (6), 2104066.

(27) Wang, J.; Gao, Y.; Chen, F.; Zhang, L.; Li, H.; de Rooij, N.; Umar, A.; Lee, Y.; French, P.; Yang, B.; et al. Assembly of Core/Shell Nanospheres of Amorphous Hemin/Acetone-Derived Carbonized Polymer with Graphene Nanosheets for Room-Temperature NO Sensing. *ACS Appl. Mater. Interfaces* **2022**, *14* (47), 53193−53201.

(28) Asher, C.; de Villiers, K. A.; Egan, T. Speciation of Ferriprotoporphyrin IX in Aqueous and Mixed Aqueous Solution Is Controlled by Solvent Identity, pH, and Salt Concentration. *Inorg. Chem.* **2009**, *48* (16), 7994−8003.

(29) Olafson, K.; Ketchum, M.; Rimer, J.; Vekilov, P. Molecular Mechanisms of Hematin Crystallization from Organic Solvent. *Cryst. Growth Des.* **2015**, *15* (11), 5535−5542.

(30) Cheng, W.; Tang, X.; Zhang, Y.; Wu, D.; Yang, W. Applications of metal-organic framework (MOF)-based sensors for food safety: Enhancing mechanisms and recent advances. *Trends Food Sci. Technol.* **2021**, *112*, 268−282.

(31) Chang, Y.; Chen, M.; Fu, Z.; Lu, R.; Gao, Y.; Chen, F.; Li, H.; Frans de Rooij, N.; Lee, Y.; Wang, Y.; et al. Building porphyrin-based MOFs on MXenes for ppb-level NO sensing. *J. Mater. Chem. A* **2023**, *11* (13), 6966−6977.

(32) Chang, Y.; Zhang, J.; Lu, R.; Li, W.; Feng, Y.; Gao, Y.; Yang, H.; Wang, F.; Li, H.; Lee, Y.; et al. Sheet-on-sheet architectural assembly of MOF/graphene for high-stability NO sensing at room temperature. *J. Mater. Chem. C* **2024**, *12* (21), 7520−7531.

(33) Mousaabadi, K.; Ensafi, A.; Rezaei, B. Simultaneous determination of some opioid drugs using Cu-hemin MOF@MWCNTs as an electrochemical sensor. *Chemosphere* **2022**, *303*, 135149−135155.

(34) Deng, Q.; Sun, P.; Zhang, L.; Liu, Z.; Wang, H.; Ren, J.; Qu, X. Porphyrin MOF Dots−Based, Function-Adaptive Nanoplatform for Enhanced Penetration and Photodynamic Eradication of Bacterial Biofilms. *Adv. Funct. Mater.* **2019**, *29* (30), 201903018.

(35) Xing, Y.; Yang, Z.; Zhao, L.; Zhang, Y.; Wei, Z.; Xing, C.; Fei, T.; Liu, S.; Zhang, T. A multisite strategy to improve room-temperature DMMP sensing performances on reduced graphene oxide modulated by N-doped carbon nanoparticles and copper ions. *Sens. Actuators, B* **2023**, *393*, 134220−134233.

(36) Ma, J.; Chen, G.; Bai, W.; Zheng, J. Amplified Electrochemical Hydrogen Peroxide Sensing Based on Cu-Porphyrin Metal−Organic Framework Nanofilm and G-Quadruplex-Hemin DNAzyme. *ACS Appl. Mater. Interfaces* **2020**, *12* (52), 58105−58112.

(37) Xiao, J.; Hu, X.; Wang, K.; Zou, Y.; Gyimah, E.; Yakubu, S.; Zhang, Z. A novel signal amplification strategy based on the competitive reaction between 2D Cu-TCPP(Fe) and polyethyleneimine (PEI) in the application of an enzyme-free and ultrasensitive electrochemical immunosensor for sulfonamide detection. *Biosens. Bioelectron.* **2020**, *150*, 111883−111890.

(38) Mao, S.; Pu, H.; Chen, J. Graphene oxide and its reduction: modeling and experimental progress. *RSC Adv.* **2012**, *2* (7), 2643−2662.

(39) Wang, Y.; Zhao, M.; Ping, J.; Chen, B.; Cao, X.; Huang, Y.; Tan, C.; Ma, Q.; Wu, S.; Yu, Y.; et al. Bioinspired Design of Ultrathin 2D Bimetallic Metal-Organic-Framework Nanosheets Used as Biomimetic Enzymes. *Adv. Mater.* **2016**, *28* (21), 4149−4155.

(40) Olafson, K.; Rimer, J.; Vekilov, P. Growth of Large Hematin Crystals in Biomimetic Solutions. *Cryst. Growth Des.* **2014**, *14* (5), 2123−2127.

(41) He, J.; Yang, H.; Zhang, Y.; Yu, J.; Miao, L.; Song, Y.; Wang, L. Smart Nanocomposites of Cu-Hemin Metal-Organic Frameworks for Electrochemical Glucose Biosensing. *Sci. Rep.* **2016**, *6*, 36637.

(42) Mi, L.; Sun, Y.; Shi, L.; Li, T. Hemin-Bridged MOF Interface with Double Amplification of G-Quadruplex Payload and DNAzyme Catalysis: Ultrasensitive Lasting Chemiluminescence MicroRNA Imaging. *ACS Appl. Mater. Interfaces* **2020**, *12* (7), 7879−7887.

(43) Chen, X.; Wang, X.; Cao, G.; Wu, Y.; Luo, H.; Ji, Z.; Shen, C.; Huo, D.; Hou, C. Colorimetric and Fluorescent Dual-Identification of Glutathione Based on its Inhibition on the 3D Ball-Flower Shaped Cu-Hemin-MOF's Peroxidase-Like Activity. *Mikrochim. Acta* **2020**, *187* (11), 601.

(44) Mousaabadi, K.; Ensafi, A.; Rezaei, B. Simultaneous Determination of Some Opioid Drugs Using Cu-hemin MOF@MWCNTs as An Electrochemical Sensor. *Chemosphere* **2022**, *303* (3), 135149.

(45) Choi, J.; Son, W.; Kim, J.; Ahn, W. Metal−Organic Framework MOF-5 Prepared by Microwave Heating: Factors to Be Considered. *Microporous Mesoporous Mater.* **2008**, *116* (1), 727−731.

(46) Romeo, A.; Castriciano, M.; Occhiuto, I.; Zagami, R.; Pasternack, R.; Scolaro, L. Kinetic Control of Chirality in Porphyrin J-Aggregates. *J. Am. Chem. Soc.* **2014**, *136* (1), 40−43.

(47) Wang, L.; Yang, H.; He, J.; Zhang, Y.; Yu, J.; Song, Y. Cu-Hemin Metal-Organic-Frameworks/Chitosan-Reduced Graphene Oxide Nanocomposites with Peroxidase-Like Bioactivity for Electrochemical Sensing. *Electrochim. Acta* **2016**, *213*, 691−697.

(48) Jiang, S.; Cheng, R.; Wang, X.; Xue, T.; Liu, Y.; Nel, A.; Huang, Y.; Duan, X. Real-time electrical detection of nitric oxide in biological systems with sub-nanomolar sensitivity. *Nat. Commun.* **2013**, *4*, 2225.

(49) Wang, Y.; Sauriat, D.; Korri, Y. Direct electrochemical DNA biosensor based on reduced graphene oxide and metalloporphyrin nanocomposite. *Sens. Actuators, B* **2017**, *251*, 40−48.

(50) Jahan, M.; Bao, Q.; Loh, K. P. Electrocatalytically Active Graphene−Porphyrin MOF Composite for Oxygen Reduction Reaction. *J. Am. Chem. Soc.* **2012**, *134* (15), 6707−6713.

(51) Xu, X.; Luo, Z.; Ye, K.; Zou, X.; Niu, X.; Pan, J. One-Pot Construction of Acid Phosphatase and Hemin Loaded Multifunctional Metal-Organic Framework Nanosheets for Ratiometric Fluorescent Arsenate Sensing. *J. Hazard. Mater.* **2021**, *412*, 124407−124414.

(52) Alizadeh, N.; Salimi, A.; Hallaj, R.; Fathi, F.; Soleimani, F. Ni-Hemin Metal-Organic Framework with Highly Efficient Peroxidase Catalytic Activity: Toward Colorimetric Cancer Cell Detection and Targeted Therapeutics. *J. Nanobiotechnol.* **2018**, *16* (1), 93.

(53) Liang, H.; Guo, L.; Cao, N.; Hu, H.; Li, H.; Frans de Rooij, N.; Umar, A.; Algarni, H.; Wang, Y.; Zhou, G. Practical room temperature formaldehyde sensing based on a combination of visible-light activation and dipole modification. *J. Mater. Chem. A* **2021**, *9* (42), 23955−23967.

(54) Xue, T.; Jiang, S.; Qu, Y.; Su, Q.; Cheng, R.; Dubin, S.; Chiu, C. Y.; Kaner, R.; Huang, Y.; Duan, X. Graphene-Supported Hemin as A Highly Active Biomimetic Oxidation Catalyst. *Angew. Chem., Int. Ed. Engl.* **2012**, *51* (16), 3822−3825.

(55) Silkoff, P. E.; Bourke, T.; Katial, R.; Ögren, E.; Szefler, S. The Aerocrine exhaled nitric oxide monitoring system NIOX is cleared by the US Food and Drug Administration for monitoring therapy in asthma. *J. Allergy Clin. Immunol.* **2004**, *114* (5), 1241−1256.

(56) Murali, G.; Reddeppa, M.; Seshendra Reddy, C.; Park, S.; Chandrakalavathi, T.; Kim, M.; In, I. Enhancing the Charge Carrier

Separation and Transport via Nitrogen-Doped Graphene Quantum Dot-TiO_2 Nanoplate Hybrid Structure for an Efficient NO Gas Sensor. *ACS Appl. Mater. Interfaces* **2020**, *12* (11), 13428−13436.

(57) Duy, L.; Noh, Y.; Seo, H. Improving graphene gas sensors via a synergistic effect of top nanocatalysts and bottom cellulose assembled using a modified filtration technique. *Sens. Actuators, B* **2021**, *334*, 129676.

(58) Hou, S.; Pang, R.; Chang, S.; Ye, L.; Xu, J.; Wang, X.; Zhang, Y.; Shang, Y.; Cao, A. Synergistic CNFs/CoS_2/MoS_2 Flexible Films with Unprecedented Selectivity for NO Gas at Room Temperature. *ACS Appl. Mater. Interfaces* **2020**, *12* (26), 29778−29786.

(59) Jeong, D.; Kim, K.; Kim, B.; Byun, Y. Characteristics of Highly Sensitive and Selective Nitric Oxide Gas Sensors Using Defect-Functionalized Single-Walled Carbon Nanotubes at Room Temperature. *Appl. Surf. Sci.* **2021**, *550* (1), 149250.

(60) Kuchi, C.; Naresh, B.; Reddy, P. In Situ TiO_2-rGO Nanocomposite for Low Concentration NO Gas Sensor. *ECS J. Solid State Sci. Technol.* **2021**, *10* (3), 037008.

(61) Jeon, J.; Kang, B.; Byun, Y.; Ha, T. High-Performance Gas Sensors Based on Single-Wall Carbon Nanotube Random Networks for the Detection of Nitric Oxide Down to the ppb-Level. *Nanoscale* **2019**, *11* (4), 1587−1594.

(62) Singh, S.; Saggu, I.; Chen, K.; Xuan, Z.; Swihart, M.; Sharma, S. Humidity-Tolerant Room-Temperature Selective Dual Sensing and Discrimination of NH_3 and NO Using a WS_2/MWCNT Composite. *ACS Appl. Mater. Interfaces* **2022**, *14* (35), 40382−40395.

(63) Madhaiyan, G.; Tung, T.; Zan, H.; Meng, H.; Lu, C.; Ansari, A.; Chuang, W.; Lin, H. UV-Enhanced Room-Temperature Ultrasensitive NO Gas Sensor with Vertical Channel Nano-Porous Organic Diodes. *Sens. Actuators, B* **2020**, *320* (NO), 128392.

(64) Nguyen, T.; Escaño, M.; Kasai, H. Nitric Oxide Adsorption Effects on Metal Phthalocyanines. *J. Phys. Chem. B* **2010**, *114* (31), 10017−10021.

(65) Nguyen, T.; Padama, A.; Escano, M.; Kasai, H. Theoretical Study on The Adsorption of NO on Metal Macrocycles, Metal = Mn,Fe,Co,Ni,Cu,Zn. *ECS Trans.* **2013**, *45* (20), 91.

(66) Li, J.; Lan, H.; Liu, H.; Zhang, G.; An, X.; Liu, R.; Qu, J. Intercalation of Nanosized Fe3C in Iron/Carbon To Construct Multifunctional Interface with Reduction, Catalysis, Corrosion Resistance, and Immobilization Capabilities. *ACS Appl. Mater. Interfaces* **2019**, *11* (17), 15709−15717.

(67) Jeong, N.; Samanta, B.; Lee, C.; Farha, O.; Hupp, J. Coordination-Chemistry Control of Proton Conductivity in the Iconic Metal−Organic Framework Material HKUST-1. *J. Am. Chem. Soc.* **2012**, *134* (1), 51−54.

(68) Zhou, S.; Jiang, L.; Zhang, J.; Zhao, P.; Yang, M.; Huo, D.; Luo, X.; Shen, C.; Hou, C. Fabrication of Cu-hemin Metal-Organic-fFrameworks Nanoflower Supported on Three-Dimensional Reduced Graphene Oxide for the Amperometric Detection of H_2O_2. *Mikrochim. Acta* **2021**, *188* (5), 160.